Suppression of antiferromagnetic order in the electron-doped cuprate T'-$La_{2-x}Ce_xCuO_{4\pm\delta}$

C. Y. Tang,[1,2,*] Z. F. Lin,[1,2,*] J. X. Zhang,[3] X. C. Guo,[1,2] J. Y. Guan,[1,2] S. Y. Gao,[1,2] Z. C. Rao,[1,2] J. Zhao,[1,2] Y. B. Huang,[4] T. Qian,[1,5] Z. Y. Weng,[3] K. Jin,[1,2,5,†] Y. J. Sun,[1,6,‡] and H. Ding[1,2,5,§]

[1]*Beijing National Laboratory for Condensed Matter Physics and Institute of Physics, Chinese Academy of Sciences, Beijing 100190, China*
[2]*University of Chinese Academy of Sciences, Beijing 100049, China*
[3]*Institute for Advanced Study, Tsinghua University, Beijing 100084, China*
[4]*Shanghai Advanced Research Institute, Chinese Academy of Sciences, Shanghai 201204, China*
[5]*Songshan Lake Materials Laboratory, Dongguan, Guangdong 523808, China*
[6]*Department of Physics, Southern University of Science and Technology, Shenzhen 518055, China*

(Received 11 June 2021; revised 28 September 2021; accepted 29 September 2021; published 14 October 2021)

We performed systematic angle-resolved photoemission spectroscopy measurements *in situ* on T'-$La_{2-x}Ce_xCuO_{4\pm\delta}$ (LCCO) thin films over the extended doping range prepared by the refined ozone/vacuum annealing method. Electron doping level (n), estimated from the measured Fermi surface (FS) volume, varied from 0.05 to 0.23, fully encompassing the superconducting dome. We observed an absence of the insulating behavior around $n \sim 0.05$ and the shift of FS reconstruction to $n \sim 0.11$ in LCCO from $n \sim 0.15$ in other electron-doped cuprates, suggesting that the antiferromagnetic order is strongly suppressed in this material. The possible explanation may lie in the enhanced next-nearest-neighbor hopping in LCCO because of the largest La^{3+} ionic radius among all the lanthanide elements.

DOI: 10.1103/PhysRevB.104.155125

In the pursuit of a grand understanding of high-temperature cuprate superconductivity, people often find the electron-doped (n-type) cuprates puzzling and somewhat awkward, mainly owing to a much more robust antiferromagnetic (AFM) phase and the absence of a pseudogap phase [1,2]. It is not clear up to now whether the electron-hole asymmetry is fundamental (i.e., due to different residing orbitals [1] or different correlation strengths caused by electron or hole charges [3,4]) or accidental (i.e., due to a band effect caused by the structural difference in the n-type cuprates [5,6]). The general formula unit of electron-doped cuprates is usually given as $Ln_{2-x}Ce_xCuO_{4\pm\delta}$, where Ln = La, Pr, Nd, Sm, Eu, or Gd with gradually decreasing ionic radius. They are the so-called T' families due to the lack of apical oxygen ions. The as-grown samples become superconducting only after a proper reduction process, which is speculated to remove apical or planar oxygen ions or to compensate Cu vacancies [7]. Among the $Ln_{2-x}Ce_xCuO_{4\pm\delta}$ systems, $La_{2-x}Ce_xCuO_{4\pm\delta}$ (LCCO) has the highest T_c and the narrowest AFM region [2,8], which may be in the closest proximity to their hole-doped counterpart $La_{2-x}Sr_xCuO_{4\pm\delta}$ (LSCO). However, the T'-LCCO can only stabilize in the thin-film form, and the underdoped film is difficult to grow in the single T' phase [7,9]. Thus, systematic experimental measurements are lacking for this material, including angle-resolved photoemission spectroscopy (ARPES) results [10].

In this paper, we adopted the two-step ozone/vacuum annealing procedure to modify the electron doping level (n) of LCCO films [2], and we performed systematic *in situ* ARPES experiments on these films. High-quality LCCO films were grown on Nb-doped $SrTiO_3$ (STO) substrates by pulsed laser deposition with Ce concentrations $x = 0.1$ and 0.19 and thickness of 150–200 nm. During the first annealing step, films were annealed at ~700 °C and the ozone partial pressure of 5×10^{-7} Torr for 30 min in an ozone-assisted molecular-beam epitaxy system. This high-temperature ozone annealing process restores the freshness of the sample surface by removing the impurities absorbed in the air and reduces the electron doping level by adding more oxygen ions into the sample. The films were subsequently annealed under a high vacuum at different temperatures between 400 and 700 °C to remove excess oxygen ions. Consequently, their electron doping levels can be continuously changed, and their electronic structures can be measured by ARPES *in situ*. The electron doping level is estimated from the measured Fermi surface (FS) volume by the Luttinger sum rule [11–14]. Using this method, we were able to measure ARPES spectra on $La_{2-x}Ce_xCuO_{4\pm\delta}$ films from $n \sim 0.05-0.23$ across the whole superconducting dome using the original films with $x = 0.1$ and 0.19. Thus, this refined ozone/vacuum annealing method can provide us a good platform to explore the doping evolution of the FS and band structure in LCCO.

For the films with $n \sim 0.05-0.19$, ARPES measurements were performed with a VG Scienta R4000 analyzer and a VUV helium plasma discharge lamp in our laboratory at the Institute of Physics. He IIα (40.8 eV) photons were used to enhance the photoelectron yield, and the base pressure of the ARPES system is 4×10^{-11} Torr. All measurements were

*These authors contributed equally to this work.
†kuijin@iphy.ac.cn
‡sunyj@sustech.edu.cn
§dingh@iphy.ac.cn

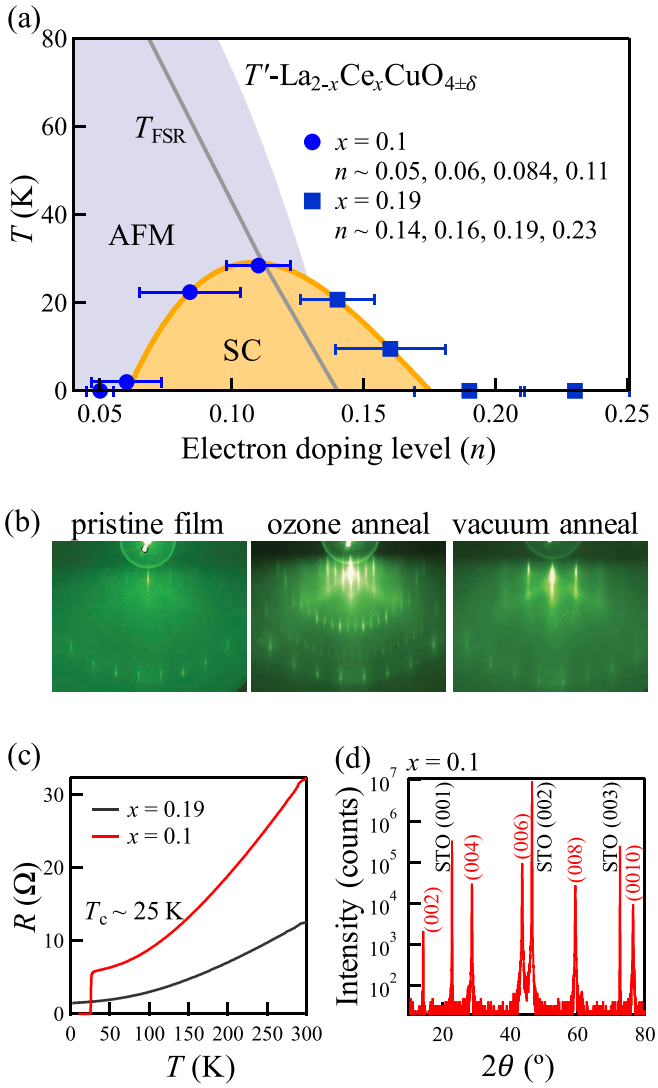

FIG. 1. (a) Phase diagram of T'-La$_{2-x}$Ce$_x$CuO$_{4\pm\delta}$ (LCCO).The superconducting dome is referenced from transport measurements, and the purple antiferromagnetic region is from angular magnetoresistance data, respectively [8,15]. The gray Fermi surface (FS) reconstruction (FSR) line is based on Hall measurements, indicating the phase transition of the FSR [16]. The blue marks represent the doping levels estimated from the FS volume of films by ozone/vacuum annealing, with the Ce concentrations x corresponding to 0.1 (dots) and 0.19 (squares). Error bars are estimated from the uncertainty of determining the nodal k_F. (b) Reflection high-energy electron diffraction patterns record the process of refreshing the film surface and tuning the doping level, and the patterns are from a pristine LCCO film exposed to air and after ozone/vacuum annealing. (c) Temperature dependence of resistivity for as-grown LCCO films on $SrTiO_3$ (STO) substrate with $x = 0.1, 0.19$. (d) X-ray diffraction pattern of a LCCO film with $x = 0.1$. The peaks of Nb-doped STO substrate are marked in black color and the (00l) peaks of T'-LCCO are marked in red.

carried out at 30 K unless otherwise specified. For the film with $n \sim 0.23$, ARPES was measured at the Dreamline beamline of the Shanghai Synchrotron Radiation Facility (SSRF), with a Scienta Omicron DA30L analyzer at ~20 K, with the photon energy of 55 eV.

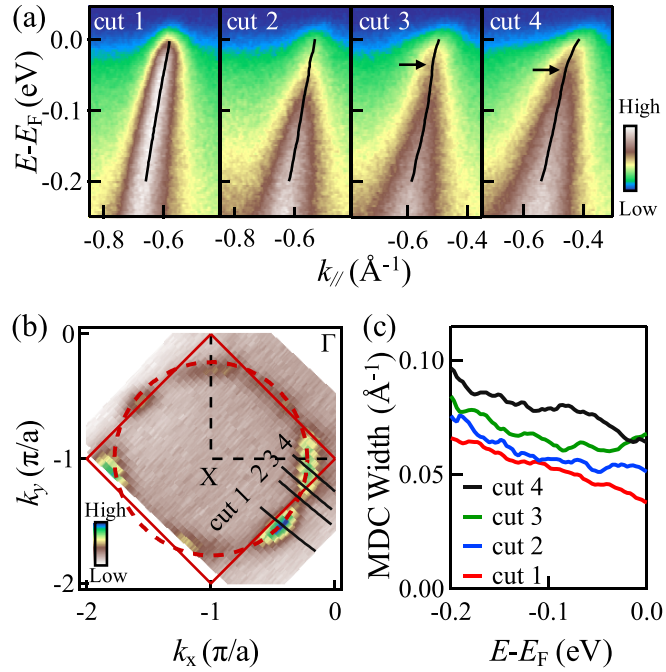

FIG. 2. (a) The representative band dispersions measured at 10 K, which are referred to as the node, the hotspot, near the hotspot, and the antinode, respectively, as indicated in (b). The black arrows in (a) indicate the positions of the kinks. (b) Fourfold symmetrized FS measured at 30 K by integrating over $E_F \pm 15$ meV; the locus of the highest intensity in the FS map is fitted by the tight-binding model, which displays as the red dashed curve. The estimated doping level is $n \sim 0.06$. The solid red lines are the antiferromagnetic Brillouin-zone boundaries. The absent spectral weight at the upper half of the FS is due to the matrix element effect. (c) The half width at half maximum of the momentum distribution curves (MDCs) for the four cuts.

Figure 1(a) is the phase diagram of LCCO from transport and angular magnetoresistance measurements [8,15,16]. The blue marks represent the doping levels of films after ozone/vacuum annealing, with the Ce concentrations x corresponding to 0.1 and 0.19. Figure 1(b) shows the reflection high-energy electron diffraction (RHEED) pattern of a pristine film and the pattern after ozone/vacuum annealing. The surfaces of *ex situ* LCCO films were contaminated by air, which can be seen from the weak RHEED pattern. After the two-step ozone/vacuum annealing process, much clearer RHEED patterns and the appearance of Kikuchi lines indicate the recovery of the freshness of sample surfaces, on which ARPES measurements can be performed afterward. Figures 1(c)–1(d) exhibit the temperature dependence of the resistivity for the as-grown $x = 0.1$ and 0.19 films and the x-ray diffraction pattern of a $x = 0.1$ sample. All these data suggest the good quality of our samples, allowing reliable ARPES measurements.

The general electronic structure at a representative doping level $n \sim 0.06$ is illustrated in Fig. 2. It can be seen in Fig. 2(b), at the cross point of the FS and AFM zone boundary, the spectral weight is suppressed, which is often referred to as the hotspot. Figure 2(a) displays the band dispersions along the four cuts indicated in Fig. 2(b) measured at 10 K. The band

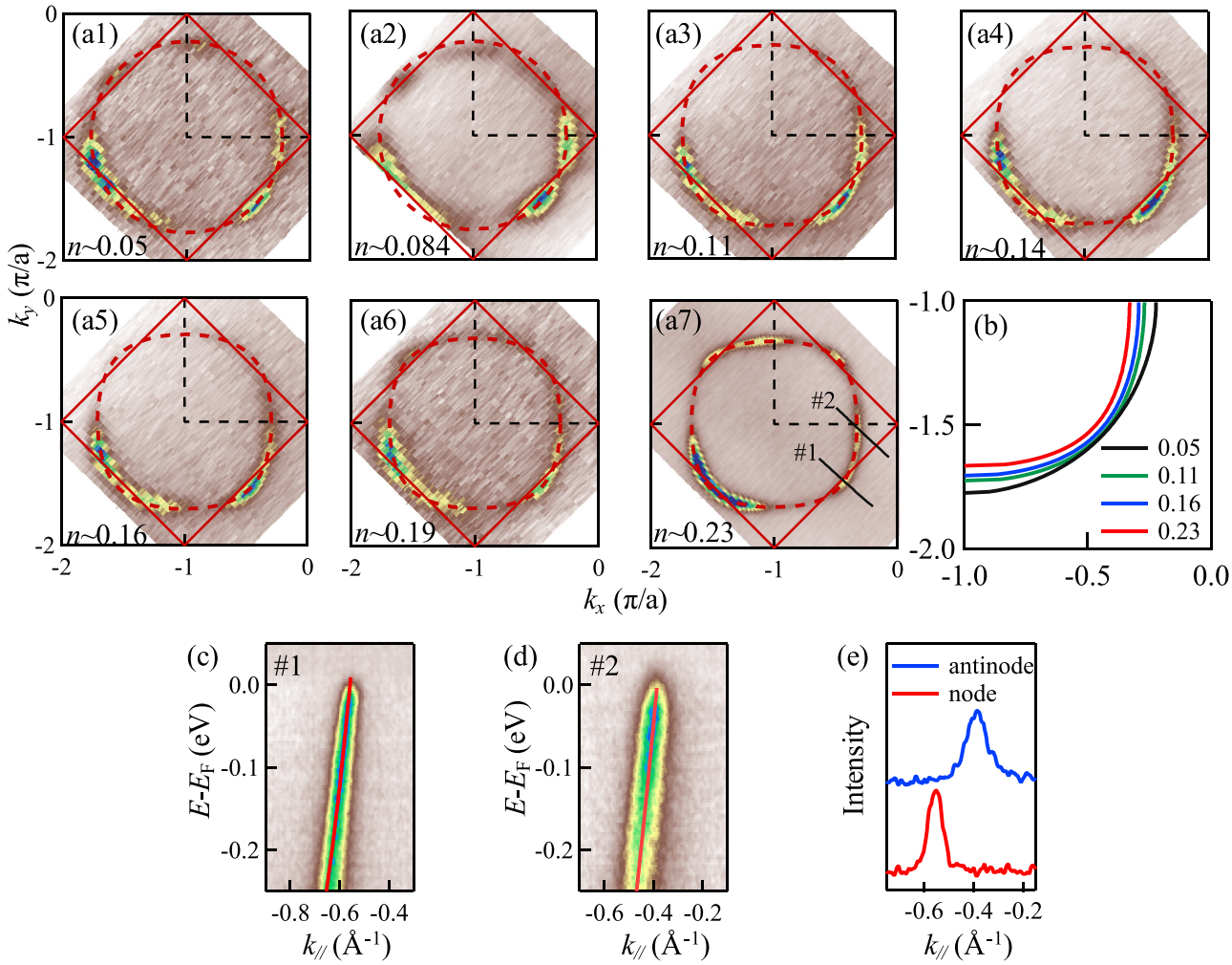

FIG. 3. (a1)–(a7) The evolution of FS for the films with $n \sim 0.05-0.23$. (b) The schematic FSs from the highly underdoped to heavily overdoped films. (c) and (d) Nodal and antinodal band dispersions as indicated in (a7) were acquired at $n \sim 0.23$. The red lines are the tight-binding fitting results with $t = 0.3$. (e) Momentum distribution curves (MDCs) at the Fermi level (E_F) for the band in (c) and (d).

dispersion at the hotspot (cut 2) displays a large gap induced by the (π, π) AFM scattering and, near the hotspot (cut 3), has a noticeable kink at the AFM zone boundary, as indicated by the black arrow. The nodal band dispersion (cut 1) remains sharp, while the antinodal band (cut 4) also displays a kink feature, sometimes attributed as the consequence of electron-boson coupling [17]. Figure 2(c) plots the half width at half maximum of the momentum distribution curves (MDCs) extracted from the four cuts. The MDC width at the antinode is larger than the one at the node, like other cuprates [17–19]. However, we should note that different slopes of the band dispersion at different momentum locations will contribute to the change of the MDC width. The overall MDC widths are relatively small, suggesting that the films are of high quality after the ozone/vacuum annealing.

The good quality of data paves a good way for studying the doping dependence of the electronic structure in LCCO. We next turn attention to the evolution of the FS. FSs for the films with $n \sim 0.05-0.23$ are displayed in Figs. 3(a1)–3(a7). The tight-binding (TB) fitted FSs from highly underdoped to heavily overdoped films are plotted in Fig. 3(b). At $n \sim 0.05$, the ARPES spectrum shows a metallic behavior with no charging gap, while transport and low-energy muon spin rotation (LE-μSR) measurements suggest an insulating AFM behavior at 0.06 [8,9,20]. The long-range AFM order is suppressed in the ozone/vacuum annealed LCCO films compared with as-grown samples, possibly resulting from higher efficiency of reducing apical oxygens by the annealing process. While the FS reconstruction (FSR) in LCCO is like other electron-doped cuprates, it should be noted that the FSR is observed only below $n \sim 0.11$, with no spectral weight near E_F at the hotspot. Moreover, the disappearance of FSR at ~0.11 at 30 K is consistent with the resistivity and Hall results [16]. This doping value is lower than that in many other electron-doped cuprates, which is ~0.15 [13,17,21,22]. ARPES measurements at electron doping levels $n \sim 0.14-0.23$ were performed on the $x = 0.19$ film, and all the spectra show a similar behavior with full circular FSs. We display the fitting result for the nodal and antinodal band dispersions at $n \sim 0.23$ in Figs. 3(c)–3(d). In the TB model, μ, t, t', and t'' represent the chemical potential, the nearest-neighbor, the next-nearest-neighbor, and the next-next-nearest-neighbor hopping integrals on the Cu-O plane, respectively. By fixing the scaled μ/t and the scaled $-t'/t$ as

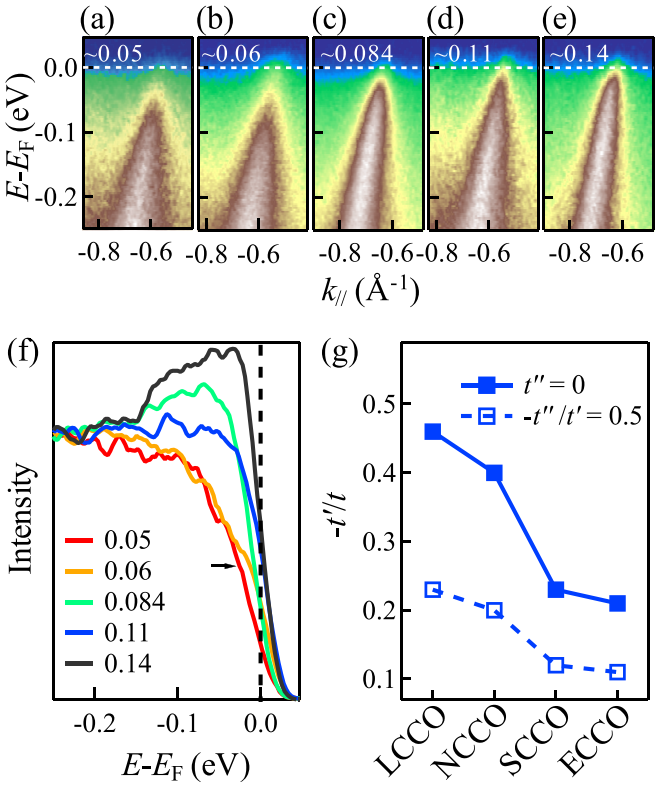

FIG. 4. (a)–(e) Doping evolution of band dispersions at the hotspot. Spectra at $n \sim 0.06$ and 0.084 were acquired at 10 K; others were measured at 30 K. The white dashed lines represent the E_F. The energy distribution curves (EDCs) at k_F are summarized in (f). The black arrow indicates the leading-edge shift is ~25 meV for $n \sim 0.05$. (g) Comparison of $-t'/t$ for different systems LCCO, NCCO, SCCO, and ECCO at their optimal doping. Solid and dashed lines reflect the assumption $t'' = 0$ and $-t''/t' = 0.5$, respectively.

for the FS at $n \sim 0.23$, the TB fitting results with $t = 0.3$ agree well with the experimental band dispersions. The well-fitted bands further support the accuracy of the estimated doping levels.

The suppression of the AFM order in LCCO can be confirmed from the following two aspects: (1) the lower doping level characterizing the FSR mentioned above, which means the AFM region is compressed as compared with other electron-doped cuprates, and (2) the quantitively smaller AFM gap at the hotspot. To get a clearer vision of the magnitude of the AFM gap, we plot the evolution of band dispersion at the hotspot from $n \sim 0.05$ to 0.14 in Figs. 4(a)–4(e). The energy distribution curves (EDCs) at k_F are summarized in Fig. 4(f). The AFM gap gradually closes as n increases, and the maximum leading-edge (LE) shift is ~25 meV at $n \sim 0.05$. However, the LE shift is ~50 meV in PLCCO at $n \sim 0.045$, and a quantitative AFM gap at the hotspot was estimated to be ~80 meV in NCCO at $x = 0.15$ [13,17,21].

There are some possible explanations for the weakening of the AFM order in LCCO. We note that previous optical and Raman experiments revealed that the charge transfer gap Δ and the AFM exchange interaction J decrease with increasing Cu-O distance [23,24]. As explained below, our results of the electronic structure in LCCO support that the AFM order is likely suppressed by the enhanced next-nearest-neighbor hopping. In a TB fit, there exist many possible sets of μ/t, t'/t, and t''/t yielding good fits to the data if there are no constraints to the parameters. There are two widely used methods to constraint the parameters: (1) set $t'' = 0$ and (2) set $-t''/t' = 0.5$ [25–27]. Here, we adapted both methods in our fits, and the two fitting results yield a similar trend, namely, the larger the Ln^{3+} ionic radius, the larger the ratio of $-t'/t$, and the ratio of $-t'/t$ for LCCO is the largest among the electron-doped cuprates, as demonstrated in Fig. 4(g) [25]. It has been suggested that $-t'/t$ is positively related to $T_{c,max}$ in both hole- and electron-doped cuprates [25–28]. In addition, the next-nearest-neighbor spin-spin exchange interaction (J') in LCCO is likely to be enhanced since $J' \sim 4(t')^2/U - 16t^4/U^3$. The larger t' enhances the AFM exchange between the next-nearest neighbors, which usually frustrates the antiferromagnetism [29,30].

We would like to point out that the LCCO samples used in this paper were grown on conducting Nb-doped STO substrates and then are annealed *in situ*, so it is difficult to obtain T_c after each procedure. It would be much better to conduct transport measurements on the samples with the same annealing procedures or combinatorial films to draw an accurate phase diagram based on electron doping level [31]. Nevertheless, since the underdoped single-phase T'-LCCO samples are difficult to be stabilized, this approach is currently the best

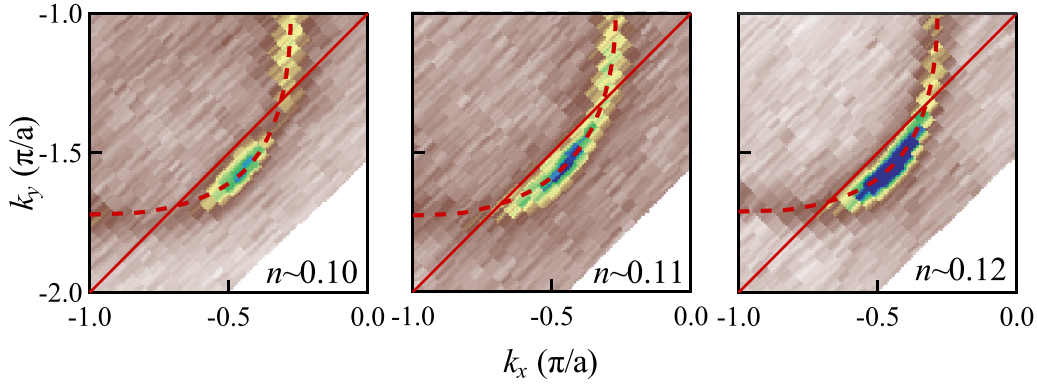

FIG. 5. The FS for $n \sim 0.10$, 0.11, and 0.12. The FS reconstruction is clear for $n \sim 0.10$ but disappears for $n \sim 0.11$ and 0.12. The samples at $n \sim 0.10$ and 0.12 are annealed from a $x = 0.15$ film.

TABLE I. Summary of the samples measured. Samples are represented as Ce_*x*#*k*, where *x* is the Ce stoichiometry, and *k* is the number of the sample. Each column from top to bottom is the ozone/vacuum annealing process for the sample. Ozone annealing procedures are marked in orange color, and other cells represent the vacuum annealing procedures. The numbers in blue are the estimated electron doping levels after each procedure.

Ce_0.1#1	Ce_0.1#2	Ce_0.15#3	Ce_0.19#4
Ozone, 5 W 40 min	Ozone, 5.1 W (728 °C), 30 min	Ozone, 5.4 W (726 °C), 25 min	Ozone, 4.3 W (728 °C), 30 min
1 W, 30 min + 2 W, 30 min ∼0.06	2 W, 8 min + 3.5 W (500 °C), 5 min ∼0.06	3 W (450 °C) 25 min ∼0.12	3.4 W (550 °C) 25 min ∼0.14
2.1 W, 20 min ∼0.084	Ozone, 5 W (743 °C), 25 min	3.6 W (560 °C) 25 min ∼0.13	3.9 W (620 °C) 25 min ∼0.16
	3.6 W (536 °C) 25 min ∼0.11	4.2 W (610 °C) 20 min + 3 W (450 °C), 15 min ∼0.15	4.3 W (660 °C) 20 min ∼0.17
	Ozone, 4.8 W (700 °C), 25 min	Ozone, 5.1 W (700 °C), 25 min	2 W, 1 h + 4.4 W (700 °C), 25 min ∼0.19
	2W, 10 min + 3.2 W (500 °C), 5 min ∼0.05	3.1 W (450 °C) 25 min ∼0.1	

way to study the doping dependence of this material [32,33]. We hope that our findings will stimulate more studies in this field both theoretically and experimentally.

In summary, using the elaborate two-step ozone/vacuum annealing method, we performed systematic ARPES measurements on electron-doped T'-LCCO. It was observed that the insulating behavior is absent at $n \sim 0.05$, probably due to the higher efficiency of removing apical oxygen ions by the annealing process. The FSR disappears at $n \sim 0.11$, indicating that the AFM order is suppressed in the annealed LCCO films. Comparing with other electron-doped systems, we find that $-t'/t$ increases as Ln^{3+} ionic radius increases, suggesting that the suppressed AFM order in LCCO may be attributed to the enhanced next-nearest-neighbor Cu hopping.

We thank K. Jiang and Y. G. Zhong for valuable discussions. This paper was supported by grants from the Natural Science Foundation of China (No. 11888101, No. 11227903 and No. U1875192), the Ministry of Science and Technology of China (No. 2016YFA0401000, No. 2017YFA0302902, and No. 2017YFA0403401), and the Chinese Academy of Sciences (No. XDB07000000 and No. XDB25000000).

APPENDIX

The FS evolution in Fig. 3 indicates that the FSR disappears at $n \sim 0.11$ in LCCO, and we also plotted the FSs for $n \sim 0.10$, 0.11, and 0.12 in Fig. 5 to further support it.

The two-step ozone/vacuum annealing procedure is employed in this paper to manipulate the electron doping of the LCCO films after the growth. Such a procedure is robust and reproducible, though the specific electron doping levels obtained after those procedures are the cumulative results of the oxygen regulation, which may be affected by the oxygen content in as-grown samples, the ozone amount, the contact resistance, etc. However, experienced experimentalists may have some skills in controlling the doping levels. Table I is the summary of the samples measured.

[1] N. P. Armitage, P. Fournier, and R. L. Greene, Rev. Mod. Phys. **82**, 2421 (2010).
[2] M. Naito, Y. Krockenberger, A. Ikeda, and H. Yamamoto, Phys. C: Supercond. Appl. **523**, 28 (2016).
[3] C. Weber, K. Haule, and G. Kotliar, Nat. Phys. **6**, 574 (2010).
[4] C. Weber, K. Haule, and G. Kotliar, Phys. Rev. B **82**, 125107 (2010).
[5] Y. Li, W. Tabis, Y. Tang, G. Yu, J. Jaroszynski, N. Barišić, and M. Greven, Sci. Adv. **5**, 7349 (2019).
[6] J. E. Hirsch and F. Marsiglio, Phys. C: Supercond. Appl. **564**, 29 (2019).
[7] P. Fournier, Phys. C: Supercond. Appl. **514**, 314 (2015).
[8] K. Jin, N. P. Butch, K. Kirshenbaum, J. Paglione, and R. L. Greene, Nature (London) **476**, 73 (2011).

[9] M. Naito and M. Hepp, Phys. C: Supercond. Appl. **357–360**, 333 (2001).
[10] H. Yamamoto, M. Naito, A. Tsukada, and S. Suzuki, Phys. C: Supercond. Appl. **412–414**, 134 (2004).
[11] H. I. Wei, C. Adamo, E. A. Nowadnick, E. B. Lochocki, S. Chatterjee, J. P. Ruf, M. R. Beasley, D. G. Schlom, and K. M. Shen, Phys. Rev. Lett. **117**, 147002 (2016).
[12] M. Horio, K. P. Kramer, Q. Wang, A. Zaidan, K. von Arx, D. Sutter, C. E. Matt, Y. Sassa, N. C. Plumb, M. Shi *et al.*, Nat. Commun. **7**, 10567 (2016).
[13] D. Song, G. Han, W. Kyung, J. Seo, S. Cho, B. S. Kim, M. Arita, K. Shimada, H. Namatame, M. Taniguchi *et al.*, Phys. Rev. Lett. **118**, 137001 (2017).
[14] C. Lin, T. Adachi, M. Horio, T. Ohgi, M. A. Baqiya, T. Kawamata, H. Sato, T. Sumura, K. Koshiishi, S. Nakata *et al.*, Phys. Rev. Research **3**, 013180 (2021).
[15] K. Jin, X. H. Zhang, P. Bach, and R. L. Greene, Phys. Rev. B **80**, 012501 (2009).
[16] T. Sarkar, P. R. Mandal, J. S. Higgins, Y. Zhao, H. Yu, K. Jin, and R. L. Greene, Phys. Rev. B **96**, 155449 (2017).
[17] J. He, C. R. Rotundu, M. S. Scheurer, Y. He, M. Hashimoto, K. Xu, Y. Wang, E. W. Huang, T. Jia, S. Chen *et al.*, Proc. Natl Acad. Sci. U.S.A. **116**, 3449 (2019).
[18] X. J. Zhou, T. Yoshida, D.-H. Lee, W. L. Yang, V. Brouet, F. Zhou, W. X. Ti, J. W. Xiong, Z. X. Zhao, T. Sasagawa *et al.*, Phys. Rev. Lett. **92**, 187001 (2004).
[19] Y.-G. Zhong, J.-Y. Guan, X. Shi, J. Zhao, Z.-C. Rao, C.-Y. Tang, H.-J. Liu, Z. Y. Weng, Z. Q. Wang, G. D. Gu *et al.*, Phys. Rev. B **98**, 140507(R) (2018).
[20] H. Saadaoui, Z. Salman, H. Luetkens, T. Prokscha, A. Suter, W. A. MacFarlane, Y. Jiang, K. Jin, R. L. Greene, E. Morenzoni *et al.*, Nat. Commun. **6**, 6041 (2015).
[21] H. Matsui, T. Takahashi, T. Sato, K. Terashima, H. Ding, T. Uefuji, and K. Yamada, Phys. Rev. B **75**, 224514 (2007).
[22] D. Song, S. R. Park, C. Kim, Y. Kim, C. Leem, S. Choi, W. Jung, Y. Koh, G. Han, Y. Yoshida *et al.*, Phys. Rev. B **86**, 144520 (2012).
[23] S. L. Cooper, G. A. Thomas, A. J. Millis, P. E. Sulewski, J. Orenstein, D. H. Rapkine, S. W. Cheong, and P. L. Trevor, Phys. Rev. B **42**, 10785 (1990).
[24] A. Sawa, M. Kawasaki, H. Takagi, and Y. Tokura, Phys. Rev. B **66**, 014531 (2002).
[25] M. Ikeda, T. Yoshida, A. Fujimori, M. Kubota, K. Ono, H. Das, T. Saha-Dasgupta, K. Unozawa, Y. Kaga, T. Sasagawa, and H. Takagi, Phys. Rev. B **80**, 014510 (2009).
[26] E. Pavarini, I. Dasgupta, T. Saha-Dasgupta, O. Jepsen, and O. K. Anderson, Phys. Rev. Lett. **87**, 047003 (2001).
[27] W. S. Lee, T. Yoshida, W. Meevasana, K. M. Shen, D. H. Lu, W. L. Yang, X. J. Zhou, X. Zhao, G. Yu, Y. Cho *et al.*, arXiv:cond-mat/0606347.
[28] Y. G. Zhong, Y. M. Chen, J. Y. Guan, J. Zhao, Z. C. Rao, C. Y. Tang, H. J. Liu, Y. J. Sun, and H. Ding, Sci. China Phys. Mech. Astron. **61**, 127403 (2018).
[29] J. Y. P. Delannoy, M. J. P. Gingras, P. C. W. Holdsworth, and A. M. S. Tremblay, Phys. Rev. B **79**, 235130 (2009).
[30] Y. Y. Peng, G. Dellea, M. Minola, M. Conni, A. Amorese, D. Di Castro, G. M. De Luca, K. Kummer, M. Salluzzo, X. Sun *et al.*, Nat. Phys. **13**, 1201 (2017).
[31] J. Yuan, Q. Chen, K. Jiang, Z. Feng, Z. Lin, H. Yu, G. He, J. Zhang, X. Jiang, X. Zhang *et al.*, arXiv:2103.08355 (2021).
[32] N. R. Poniatowski, T. Sarkar, S. DasSarma, and R. L. Greene, Phys. Rev. B **103**, L020501 (2021).
[33] R. L. Greene, P. R. Mandal, N. R. Poniatowski, and T. Sarkar, Annu. Rev. Condens. Matter Phys. **11**, 213 (2020).